Journal of Catalysis 394 (2021) 416–428

Contents lists available at ScienceDirect

Journal of Catalysis

journal homepage: www.elsevier.com/locate/jcat

Finding the active species: The conversion of methanol to aromatics over Zn-ZSM-5/alumina shaped catalysts

Irene Pinilla-Herrero [a,b,*], Elisa Borfecchia [b,c], Tomás Cordero-Lanzac [a], Uffe V. Mentzel [b], Finn Joensen [b], Kirill A. Lomachenko [d], Silvia Bordiga [c], Unni Olsbye [a], Pablo Beato [b,*], Stian Svelle [a,*]

[a] Center for Materials Science and Nanotechnology (SMN), Department of Chemistry, University of Oslo, Blindern, Oslo 0315, Norway
[b] Haldor Topsøe, A/S Kgs. Lyngby 2800, Denmark
[c] Department of Chemistry, INSTM Reference Center and NIS Interdepartmental Center, University of Turin, Via Giuria 7, I-10135 Turin, Italy
[d] European Synchrotron Radiation Facility, 71 avenue des Martyrs, CS 40220, Grenoble Cedex 9 38043, France

ARTICLE INFO

Article history:
Received 23 June 2020
Revised 7 October 2020
Accepted 17 October 2020
Available online 2 November 2020

Keywords:
Zeolite
Extrudate
Binder
XAS
X-ray absorption spectroscopy
Methanol to gasoline

ABSTRACT

The Zn-loaded zeolite ZSM-5 is an active and promising catalyst for the conversion of methanol to aromatics with high yield. In this work, we have investigated the catalytic performance of shaped Zn-ZSM-5/alumina catalysts in this reaction at industrially relevant pressures. This has been combined with extensive characterization to identify the active Zn species. It is clear that the introduction of Zn leads to an improved catalyst lifetime when the reaction is carried out at elevated pressure. A clear shift from reaction pathways leading to alkane formation to pathways leading to molecular hydrogen formation during the production of aromatics is observed. For industrial catalysts, Zn incorporation is conveniently carried out by impregnation after shaping. A significant migration of Zn into the zeolite ion exchange positions is observed upon calcination of impregnated catalysts, and it is these species that are active for the reaction. At high Zn loadings, $ZnAl_2O_4$ species observable by X-ray absorption spectroscopy, but not detectable by diffraction, are formed in the alumina binder.

1. Introduction

Zeolites and zeotypes are extensively studied inorganic materials due to their practical application as heterogeneous catalysts for several industrial processes [1–6]. Among these applications, the methanol-to-hydrocarbons conversion processes (MTH) have acquired remarkable importance in the last decades, as these are a promising nonpetroleum alternative for the production of high-octane gasoline or base chemicals such as short-chain olefins or light aromatics [7–9]. In fact, it is the versatility of the MTH technologies, together with the possibility of producing methanol from a wide variety of carbon sources, that makes these processes so important, especially in regions with a limited oil supply, but an abundance of other carbon resources, including coal or natural gas and also biomass, or more recently CO_2, as renewable carbon sources [10–14]. Lately, there has been renewed interest in the production of aromatics from methanol, since aromatics are extensively used industrial intermediates and their consumption is expected to grow in the near future [15]. The incorporation of transition metals into zeolites has been proven to be an efficient strategy to tune the MTH reaction mechanism toward the formation of aromatics: methanol to aromatics (MTA) [16–21]. Among several combinations of zeolites and transition metals, ZSM-5 is the zeolite providing the most promising MTH performance and Zn is one of the metals with the highest promoting capacity toward aromatics. In such a bifunctional catalytic system, the Brønsted acid sites (BAS) and Lewis acid sites (LAS) of the zeolite catalyze the methanol transformation into hydrocarbons. The zeolite framework provides the system with shape selectivity properties, and the extra Lewis acid sites from the transition metal add an additional dehydrogenation activity. In this way, aromatization of olefins, which involves cyclization reactions and hydrogen loss (dehydrogenation or hydrogen transfer), can be favored by that extra dehydrogenation functionality, producing aromatics and hydrogen instead of alkanes as hydrogen-rich reaction by-products.

Several of the MTH technologies are ready for commercial operation, and production plants for different hydrocarbons have been started up in the last decades [22–27]. This growth has happened hand in hand with very intensive research on the processes and the catalysts [7,9,28–38]. However, most of the fundamental research has been done using pure zeolites as catalysts. In contrast, structuring and shaping are necessary for the industrial utilization

* Corresponding authors.
E-mail addresses: i.p.herrero@kjemi.uio.no (I. Pinilla-Herrero), pabb@topsoe.com (P. Beato), stian.svelle@kjemi.uio.no (S. Svelle).

https://doi.org/10.1016/j.jcat.2020.10.024
0021-9517/

of zeolites, since a powdered catalyst is not a viable option for large-scale operation [39]. Due to the low self-binding properties of the zeolites, additives or inorganic binders are used for the shaping. This adds a complexity level and, even if pure zeolites are relatively well understood, shaped catalysts have been much less intensely investigated in the regular scientific literature related to MTH processes [1,40]. Binders are used to disperse the zeolites and provide assembling properties and the physical resistance necessary for their industrial use. Commonly, commercially available silica, alumina, or clays are used for this purpose. Although binders are often perceived as inert components, it is well known that they can influence activity, mass transfer properties, and coking phenomena. Moreover, they can represent a source of poisoning species or other mobile species that may even alter the nature of the zeolites [41–44].{Shoinkhorova, 2019 #338}

In preparing a potential industrial catalyst for the MTA process, a transition metal (Zn in our case) must be incorporated into the zeolite/binder system, making the material even more complex. As an important complicating factor, we point out that impregnation before shaping/binding is not practical beyond the laboratory scale. The promoting effect of Zn is known to be dependent not only on the amount of Zn, but also on the type of Zn species and the location of the metal in the catalyst. Zn species in the exchange position of the zeolite are quite active as dehydrogenation centers [17,21,45]. Determining with certainty both the Zn location and the nature of the metal species in pure zeolites is already quite challenging due to the spectroscopic quietness of Zn, and extensive characterization is required. When a shaped material is the subject of study, the situation becomes even more complicated. The general effects of shaping on methanol-to-hydrocarbons catalysts have been discussed by Michels et al. [43] and Shoinkhorova et al. [44]. For this type of catalyst, Zn species are likely to be different from those existing in pure zeolites. Moreover, the metal can be incorporated either into the zeolite or onto the binder or—most likely—distributed between both, presumably having different effects depending on the location within the shaped material. Thus, the characterization should be targeted toward determining the Zn location as the first and most critical question.

In this work, we aim to study the effect that Zn has on MTA performance for real catalysts and how the dehydrogenation activity varies depending on the location of Zn, type of sites, and Zn content. With this purpose, we have produced a spherelike catalyst by spray-drying a slurry containing ZSM-5 and alumina. These spheres were later impregnated or ion-exchanged to incorporate Zn. Incorporating Zn into the zeolite before spray-drying would simplify the problem, but since fine powders are not easy to deal with on a large scale, impregnation after shaping is a more realistic industrial approach. To understand the nature of these impregnated shaped catalysts, it is useful to compare them with the pure zeolite (active phase) and with pure alumina samples (binder). Thus, those two materials are used in the study for comparison. We have investigated the catalytic performance of these materials for the conversion of methanol to aromatics. However, due to the complex MTA chemistry, the materials have been investigated also as dehydrogenation catalysts for the conversion of cyclohexane and for dehydrogenation and cyclization using 1-heptene as reactant as relevant model reactions. These testing results are discussed against extensive characterization data, including scanning electron microscopy (SEM), nitrogen adsorption, powder X-ray diffraction (PXRD), Fourier transform infrared spectroscopy (FTIR), and X-ray absorption spectroscopy (XAS). Our main objective is ultimately to understand which kinds of metal sites are formed and how they are distributed between the zeolite component and the binder phase within the shaped catalysts and ultimately how this affects the catalytic performance.

2. Experimental

2.1. Catalyst preparation

Three series of catalysts were prepared by incorporating Zn (by impregnation or ion exchange) into three parent materials: pure ZSM-5 samples, spray-dried zeolite/alumina catalysts, and spray-dried alumina. A sample list and details on the Zn incorporation are provided in Table 1.

The parent pure zeolite used was commercial ZSM-5 with Si/Al = 40 (CBV-8014, Zeolyst International). The spherically shaped zeolite/alumina sample, on the other hand, was prepared by spray-drying a slurry with 30% total dry matter. This slurry was made from H-ZSM-5 zeolite (40% of the dry weight, CBV-8014, Zeolyst International) with alumina (60% of the dry weight, Catapal B). First, the zeolite was mixed with water corresponding to twice the weight of the zeolite. Second, Catapal B was mixed with a 2% solution of nitric acid made using the remaining water. These slurries were then stirred to get homogeneous mixtures and mixed to form the final slurry. The slurry was aged for 30 min before spray drying. The spray-dried material thus obtained was calcined in static air at 550 °C using a 5-h heating ramp and a 5-h hold time.

As mentioned before, Zn was incorporated into the parent solids by impregnation or ion exchange. In the case of the zeolite/alumina spray-dried material, both incorporation methods were used and compared (Table 1). Ion exchange was carried out three times at 80 °C using excess 0.15 M solution of $Zn(NO_3)_2$, and the obtained sample was calcined at 550 °C for 5 h. In the case of the samples prepared by impregnation, the desired amounts of Zn (1% and 10% of the solid weight) were dissolved in a volume of water corresponding to the pore volume of the solid, as calculated from N_2 physisorption experiments. The resulting solution was added dropwise to the solid, resulting in a wet solid in which, as planned, all the solution was absorbed. The Zn-containing pure zeolite sample used for comparison was prepared by ion exchange according to the procedure described in detail in [21]: the zeolite was exchanged three times with excess $Zn(NO_3)_2$ at 80 °C and then calcined at 450 °C for 2 h. Since pure alumina does not have any cations to be exchanged, Zn-containing samples were prepared only by impregnating the parent spray-dried alumina, following the same procedure as described for the zeolite/alumina samples.

2.2. Catalyst characterization

The particle size and size distribution of the materials were analyzed by SEM, using an FEI XL30 electron microscope with a field emission gun operated at 15 kV. The calcined zeolite samples were placed on aluminum stubs with double-sided carbon tapes. To minimize charging, the samples were coated with a thin layer of carbon (approximately 30 nm in thickness).

Table 1
Sample list, approximate Zn content, and experimental details for the incorporation of Zn into the different solids.

Sample	Parent material	Zn incorporation method	
		Impregnation	Ion exchange
Z-Parent	HZSM-5	–	–
Z-3IE			3 times
ZB-Parent	HZSM/Alumina	–	–
ZB-1Zn		1%	–
ZB-10Zn		10%	–
ZB-3IE		–	3 times
B-Parent	Alumina	–	
B-1Zn		1%	–
B-10Zn		10%	–

X-ray diffractograms were recorded using a Siemens Bruker D500 instrument in Graff–Brentano geometry with Cu$K\alpha_1$ radiation (k = 1.5406 Å).

The chemical composition of the calcined samples was studied by ICP-OES using a Rigaku Supermini200 WD-XRF instrument, applying an analytical method based on DS/EN/ISO 12677.

Adsorption properties of all the materials were evaluated by nitrogen adsorption–desorption measurements performed at the nitrogen boiling point (-196 °C) on a Bel Belsorp-mini II instrument. Before the measurements, the samples were pretreated under vacuum for 1 h at 80 °C and then for 3 h more at 300 °C. Surface area and pore volume values were calculated using the BET equation and *t*-plot method, respectively [46,47].

Fourier transform infrared spectroscopy (FTIR) experiments were carried out using a Bruker Vertex 80 instrument in transmission mode equipped with a mercury cadmium telluride (MCT) detector and using a resolution of 2 cm^{-1}. Pyridine was used as a base probe molecule, but before they were dosed, samples were pretreated under vacuum (<10^{-5} mbar) at 450 °C for 1 h (temperature ramp to the set point: 3 °C/min). Once pretreated and exposed to pyridine, samples were outgassed at 200 °C to remove the excess and the physically adsorbed pyridine. The areas of the bands at 1544 and 1455 cm^{-1} were used for quantification of the BAS and LAS, respectively, using the integrated molar extinction coefficient reported previously [48].

Zn *K*-edge XAS experiments were performed at the BM23 beamline [49] of the European Synchrotron Radiation Facility (ESRF, Grenoble, France). Catalysts of the series ZB (Table 1) were carefully ground to powder and then prepared in the form of self-supporting pellets of optimized mass and thickness for XAS in transmission mode. For the catalysts with Zn content close to 1 wt% (namely *ZB-IE3* and *ZB-1Zn*), we employed ca. 140 mg of powder, resulting in edge jumps $\Delta\mu x \sim 0.2$ with total absorption after the edge $\mu x \sim 2.5$. For the catalyst with Zn 10 wt% (namely *ZB-10Zn*), we employed ca. 75 mg of powder, obtaining an edge jump $\Delta\mu x \sim 1.3$ with total absorption after the edge $\mu x \sim 2.5$. All the samples were characterized in their as-prepared state at RT in air. The two catalysts with Zn ~ 1 wt% were further activated at 400 °C inside a dedicated glass cell equipped with Kapton windows, which allowed measurements under a controlled atmosphere. For activation, the catalysts were first outgassed in vacuum at 400 °C for 1 h and then exposed for 1 h to 100 mbar of pure O_2 at the same temperature. Once activated, the samples were cooled under vacuum and measured at RT inside the same glass cell.

Zn *K*-edge XAS spectra were collected in transmission mode, using a Si(1 1 1) double-crystal monochromator. The incident (I_0) and transmitted ($I_{1,2}$) X-ray intensities were collected by ionization chambers filled with He/Ar mixtures. A third ionization chamber (I_2) was used for the simultaneous collection of the XAS spectrum of a Zn metal foil for energy calibration purposes [50]. Rejection of higher harmonics was performed by two flat Si mirrors positioned at 2.5 mrad with respect to the incident beam. XAS scans were acquired in the range 9500–10,635 eV, with an energy step of 5 eV in the pre-edge region, of 0.2 eV in the XANES region, and a constant k step of k = 0.035 $Å^{-1}$ in the EXAFS region. Integration time was 1 s/point in the XANES region, while it increased quadratically from 1 to 4 s/point in the EXAFS region, globally resulting in ca. 25 min/scan. To characterize each sample, we acquired four or three consecutive XAS scans for catalysts with Zn 1 and 10 wt%, respectively. After energy alignment and normalization to the edge-jump using the Athena software from the Demeter package [51], the four $\mu x(E)$ curves were averaged, after checking for signal reproducibility. The corresponding k^2-weighted $\chi(k)$ functions were Fourier transformed (FT) in the range Δk = 2.3–11.0 $Å^{-1}$.

To assist the interpretation of the XAS results, we also collected Zn *K*-edge XAS data for selected model systems. These included hydrated Zn(II), obtained by measuring the XAS spectrum of a 50 mM aqueous solution of $Zn(NO_3)_2$, as well as the pure Zn-exchanged zeolite component (Z-3 E), measured after activation at 420 °C in O_2, as described in more detail in our previous studies [21,52]. Moreover, to assess the local properties of Zn ions in the sole binder component, we characterized the two Zn-impregnated alumina samples (B-1Zn and B-10Zn) by XAS. XAS spectra for the latter materials were collected at RT in air, using the same data collection strategies and parameters described above for the investigated zeolite/alumina systems.

We employed these reference spectra also for a linear combination fit (LCF) analysis of the XANES spectra collected for as-prepared and activated ZB-type catalysts. LCF analysis was performed in the energy interval 9643–9713 eV, using Athena [51]. Each experimental XANES, $\mu^{EXP}(E)$, was fitted as a linear combination of three reference XANES spectra, $\mu_i^{REF}(E)$: $\mu^{LCF}(E) = w_1\,\mu_1^{REF}(E) + w_2\,\mu_2^{REF}(E) + w_3\,\mu_3^{REF}(E)$, optimizing the weights w_i for each reference spectrum. $\mu_1^{REF}(E)$ and $\mu_2^{REF}(E)$ were selected to represent zeolite-related Zn species in the form of hydrated Zn(II) complexes and dehydrated framework-coordinated Zn ions (modeled by the spectrum of activated Z-3IE). Conversely, $\mu_3^{REF}(E)$ was aimed at modeling the binder-related Zn: in this case we employed as a reference B-1Zn or B-10Zn, using the Zn-loading comparable with each analyzed experimental spectrum. LCF was performed by imposing $0 \le w_i \le 1$, but without constraining the sum of the weights to unity, $\Sigma_i w_i = 1$. The best-fit values of $\Sigma_i w_i$ were instead examined as an additional indicator of the LCF quality. For each analyzed scan, the corresponding LCF *R*-factor was computed as $\Sigma_j [\mu_{\cdot}^{EXP}{}_j(E) - \mu_{\cdot}^{LCF}{}_j(E)]^2 / \Sigma_j [\mu_{\cdot}^{exp}{}_j(E,)]^2$, where j denotes each experimental point in the fitted energy range (9643–9713 eV); *R*-factor = 0 corresponds to the ideal reproduction of the experimental curve, $\mu^{EXP}(E) \equiv \mu^{LCF}(E)$.

2.3. Catalytic testing

For the conversion of methanol to hydrocarbons, a commercial Microactivity Effi fixed bed reactor constructed by PID Eng&Tech was employed. The catalytic tests were carried out using a continuous-downflow fixed-bed stainless steel tubular reactor with an inner diameter of 4.5 mm and a total length of 304.8 mm. The reactor has a porous plate (Hastelloy C, 20 μm) designed to ensure that the catalyst bed remains in the same position and inside the isothermal zone of the furnace. Aiming to simulate industrial conditions, 400 °C and a total pressure of 20 bar were used in all the cases. The Microactivity unit was fully automated and controlled from a PC, and the temperature of the reactor was controlled and monitored using a multipoint thermocouple placed in the lower part of the catalyst bed, above the porous plate. Two points were selected for temperature measurement: first at 5 mm above the frit (control and measurement), and second at 30 mm above the frit (only for measurement purposes). This was designed to ensure isothermal conditions along the catalyst bed. Nitrogen was used as an inert diluent gas, and the flow rate was adjusted by a mass flow controller. Methanol was fed as a liquid from a pressurized vessel using a Coriolis flow controller, and then vaporized and mixed with the nitrogen in a preheater at 190 °C, generating a gas mixture with a constant molar percentage of methanol of 10%. In a typical test, 500 mg of catalyst (pellet size of 250–420 μm, bed height 3.9 cm) was used and a methanol flow rate of 2.5 g/h (diluted in nitrogen, 260 N mL/min) was selected to obtain a weight hourly space velocity (WHSV) of 5 h^{-1}. In all cases, tests were performed in excess of catalyst and 100% conversion was reached. Before each reaction, catalysts were pretreated at atmospheric pressure to remove any traces of water or organic

molecules that might be adsorbed in the zeolite pores. In a first step, temperature was ramped up to 550 °C, exposing the catalysts to a 20% O_2 80% N_2 flow, and then the flow was changed to 80% O_2 and 20% N_2 and the temperature was kept at 550 °C for 1 h. Finally, any excess of O_2 was flushed out with 100% N_2 flow while the system was cooled to reaction temperature. The reactor effluent stream was depressurized and analyzed on line by gas chromatography using an Agilent 6890 A instrument equipped with a flame ionization detector (FID) and a Supelco SPB-5 capillary column with dimensions of 60 m × 0.53 mm × 3 μm.

To study the dehydrogenation and cyclization activities of the catalysts, samples were tested for the conversion of cyclohexane and 1-heptene. These experiments were carried out in a fixed-bed U-shaped reactor with inner diameter 6 mm operated at atmospheric pressure and 400 °C. The temperature was monitored during the reaction using a thermocouple covered with a 3-mm-wide quartz sheath located in the lower part of the catalyst bed in contact with the catalyst. Typically, 90 mg of catalyst (pressed and sieved into 250 to 420 μm particles) was used after pretreatment in situ by heating in 20% O_2 in He to 550 °C and exposure to 80% O_2 flow for 1 h at the same temperature. Both cyclohexane and 1-heptene were fed by flowing helium through a flask of boiling reactant, and the saturated steam was subsequently passed through a water-cooled condenser kept at a controlled temperature. An extra line with pure He was used to dilute the reactant feed and adjust the total flow to the reactor to 17 mL/min for all the experiments. The reactant flows were set to have the same equivalent carbon concentration for all the experiments, instead of trying to maintain the space velocity between experiments with different reactants. Thus, in the case of cyclohexane, 3.6 mL/min of He was flowed while the condenser connected to the saturator was kept at 35 °C, giving a final partial pressure of cyclohexane of 43 mbar (which results in a WHSV of 1.7 h^{-1}), and for n-heptene, on the other hand, 4.4 mL/min of He was passed through the saturator at 37.5 °C to obtain a partial pressure of n-heptene of 37 mbar (WHSV = 2.0 h^{-1}) The reactor effluent was analyzed on line by gas chromatography using an Agilent 7890 instrument equipped with an FID and a Restek Rtx-DHA-150 column.

3. Results and discussion

3.1. Catalytic performance for the conversion of methanol to aromatics

We focus here on the performance of the shaped Zn-loaded materials prepared by different methods (impregnation after shaping and ion exchange after shaping) and with different Zn loadings. A detailed discussion of the role of Zn loading in neat powdered ZSM-5 catalysts is presented in our previous work [21]. Fig. 1, top panel, shows the conversion to hydrocarbons for the shaped material when tested at WHSV = 3 h^{-1}, $T_{reaction}$ = 400 °C, methanol partial pressure 1 bar, and total pressure 20 bar. It appears that 1 wt% Zn is insufficient to influence the lifetime of the materials significantly. Repeated experiments showed that the reproducibility (evaluated by the time required to reach 50% conversion) is ± 6%, demonstrating that the minor differences between the parent and the 1 wt% Zn catalysts are indeed insignificant. A further increase in Zn loading to 10 wt% by impregnation of the spheres clearly leads to an improvement in catalyst lifetime. An impregnated sample with 5 wt% Zn (not otherwise included in the further characterization and discussion) displayed an intermediate lifetime, verifying that the effect is systematic. We note that the opposite effect, a reduced lifetime upon Zn loading, was observed for a series of ion-exchanged powdered zeolites tested at 1 bar total pressure [21]. This will be elaborated below.

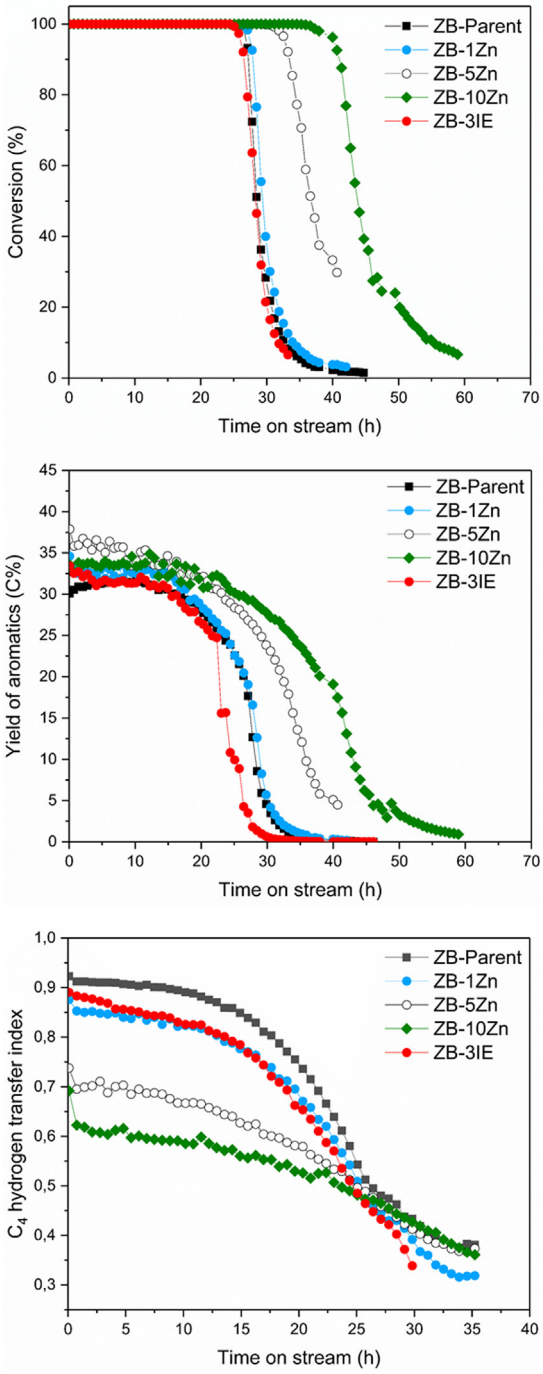

Fig. 1. Conversion of methanol to aromatics as a function of time on stream over different-shaped catalysts (Table 1) at WHSV = 5 h^{-1}, $T_{reaction}$ = 400 °C, methanol partial pressure 1 bar, and total pressure 20 bar. Top panel: conversion; middle panel: yield of aromatics; bottom panel: C_4 hydrogen transfer index.

The middle panel of Fig. 1 shows the yield of aromatics against time on stream. It appears that the yield of aromatics depends primarily on the conversion, and that only a marginal increase is seen for the 5 and 10 wt% Zn catalysts at 100% conversion. The C_4 hydrogen transfer index (C_4-HTI), defined as the ratio of paraffinic C_4 to total C_4, is shown in the bottom panel of Fig. 1 and provides more information. See the Supplementary Material for a detailed example describing the changes in paraffin/olefin ratio observed for the Zn-containing catalysts. It is evident that the C_4-HTI decreases substantially and systematically as the Zn content is increased. The

implication is that whereas the yield of aromatics increases only marginally with Zn content, the aromatization mechanism is substantially affected. By a simple argument based on the fixed H/C stoichiometry of the total products (the H/C ratio must be 2), there must be a shift from hydrogen transfer reactions leading to paraffin formation to reaction steps leading to the formation of molecular hydrogen with increasing Zn content. Note that molecular hydrogen is detectable in the effluent for the Zn-containing catalysts, as shown in the Supplementary Material. This proves the validity of the hydrogen transfer index as a relevant descriptor for the mechanisms by which the aromatics are formed. Note also that the total amount of C_4 formed is fairly constant at 20 C% at 100% conversion for all experiments. The same shift in mechanism, also inferred from the C_4-HTI, was observed in our previous experiments using powdered zeolites at 1 bar total pressure. This allows us to comment on the seemingly opposite behavior seen for the catalyst lifetime when comparing tests at elevated pressure (present work) and ambient pressure (previous work) [21].

At low pressures, we see an increase in aromatics yield, a reduction in lifetime, and a shift toward molecular hydrogen formation with increasing Zn content. It is straightforward to associate coke formation with aromatics formation, and thus a shorter lifetime at high Zn loadings when the yield of aromatics is high. At high testing pressures, however, the aromatics yield is largely unaffected, the lifetime is increased, and the same shift in mechanism is seen. It thus appears that pressure alone is sufficient to increase the aromatics yield. At a nearly constant yield of aromatics, one could reasonably assume that the coke selectivity is correspondingly little affected. This does not, however, account for the *increase* in lifetime. We therefore speculate that at higher testing pressure, the hydrogen produced at high Zn loadings somehow attenuates the coking. It has recently been established that even protonic zeolites display longer lifetimes in the presence of molecular hydrogen [53,54], and we suspect that either the acid sites or the active Zn species contribute to this effect when the partial pressure of hydrogen in the effluent is comparatively high.

The experimental data presented in Fig. 1 and discussed above serve to demonstrate that we have prepared improved MTA catalysts by Zn incorporation by impregnation of the ZSM-5/alumina spheres, and the remainder of the article will be devoted to an elucidation of the responsible active Zn species.

3.2. Location of Zn and identification of the nature of Zn species

To understand how Zn is incorporated into the complex shaped materials, the series of samples prepared from different parent solids (pure zeolite, shaped zeolites, and pure alumina) and with different Zn content (Table 1) have been studied using a variety of characterization methods. The main material under study, the spray-dried ZSM-5/alumina, was analyzed by SEM to examine the morphological characteristics of the obtained solids. From the SEM micrographs in Fig. 2, it is clear that most of the particles are sphere- or mushroom-like and that particle size distribution is rather narrow. Since the spray-drying method is by definition a quick drying of a slurry in cyclonic circulating hot air, all the particles have a smaller or larger hole caused by the evaporation of water from the solid. Impregnation and ion exchange do not lead to visible changes in the microscope, and SEM characterization of the parent powdered zeolite is presented elsewhere [21].

The chemical composition of the calcined Zn-containing solids was determined by ICP-OES, aiming to evaluate if the incorporation of Zn had been successful and to compare Zn content between samples. In our experience, zeolites easily incorporate Zn in the ion exchange positions up to a certain content [21], and normally, for the impregnated samples, all the Zn in the solution in contact with the solid is incorporated. Comparing ion-exchanged samples (Z-3IE and ZB-3IE), the amount of Zn incorporated into the shaped catalyst (ZB) is significantly lower than that in the pure zeolite (Table 2). This observation is reasonable, considering that the zeolite content in ZB-3IE is 40% of the total weight of the sample, so the number of aluminum/Brønsted sites available for ion-exchange is less than half. In fact, considering the elemental analysis results, 44% of the aluminum sites in the pure zeolite (Z-3IE) have been exchanged with Zn and, if we assume that all the Zn (0.08 mmol/g) is incorporated into the zeolite exchange sites of the shaped material (ZB-3IE), 44% of the zeolite aluminum sites of this sample have also been exchanged with Zn. Considering the (partly coincidentally) good correlation of the numbers, one could be tempted to hypothesize that using this incorporation method, Zn is mainly directed to the zeolite exchange positions instead of being randomly distributed between the zeolite and the binder. However, further studies providing more conclusive proof of the exact location and nature of Zn in the shaped catalysts are necessary to verify that.

Looking now at the impregnated samples and provided that the pore volume calculations were done for pretreated samples and that, for the impregnation procedure, hydrated materials were used (this slightly affect the amount of solid weighed in), in all cases the final Zn content is very close to the theoretical one (Tables 1 and 2).

It is known from previous studies that the presence of metal ions in the channels of the zeolite does not cause remarkable changes in the adsorption capacity of the materials. However, very high Zn content, as for our samples, could give rise to the formation of Zn agglomerates, which in turn could provoke spatial restrictions in the porous solids; so it is important to observe if the adsorption properties of the materials change upon Zn incorporation. All the samples, parent and Zn-containing ones, were studied by N_2 physisorption measurements in order to evaluate any variation in the textural properties or adsorption capacity. The nitrogen isotherms of all the pure zeolites (Z-*x* series) and the zeolite/binder materials (ZB-*x*) show quite a steep increase in the nitrogen uptake at relatively low partial pressures of nitrogen (Fig. 3). The pure zeolites (left panel) have isotherms with a very typical shape of microporous materials (type I–II). However, the alumina samples (right) have quite different isotherms, showing very limited nitrogen uptake at low partial pressures with a quite rapid increase in the volume of nitrogen adsorbed when the nitrogen partial pressure is high (isotherms type IV–V). Such behavior is characteristic of nonmicroporous materials. Finally, the shaped catalysts display intermediate behavior, with both hysteresis and a fairly steep increase in nitrogen uptake at intermediate nitrogen partial pressures (isotherms of type IV), which shows that there are also some pores or interparticle spaces in the range of the meso–macropores [55]. These differences can also play a role in the incorporation of Zn, as the formation of larger agglomerates is more feasible in materials with a greater nonmicroporous surface.

Surface area and pore volume values were calculated from the isotherms and are collected in Table 3. The variation of the surface area and pore volume in pure zeolites exchanged with Zn has been studied previously [21], and from this previous study, it is clear that neither the surface nor the pore volume vary systematically upon Zn incorporation, so it was concluded that the presence of Zn clusters or ZnO agglomerates in the micropores of the zeolites was not likely and that Zn ions in the zeolite exchange sites were not causing any special restriction. For the shaped catalysts or alumina samples with low Zn loading, this situation appears to persist. However, for the 10 wt% Zn loading samples, the situation changes. In both these cases, there is a significant reduction of the surface area with the incorporation of Zn into the materials (Table 3).

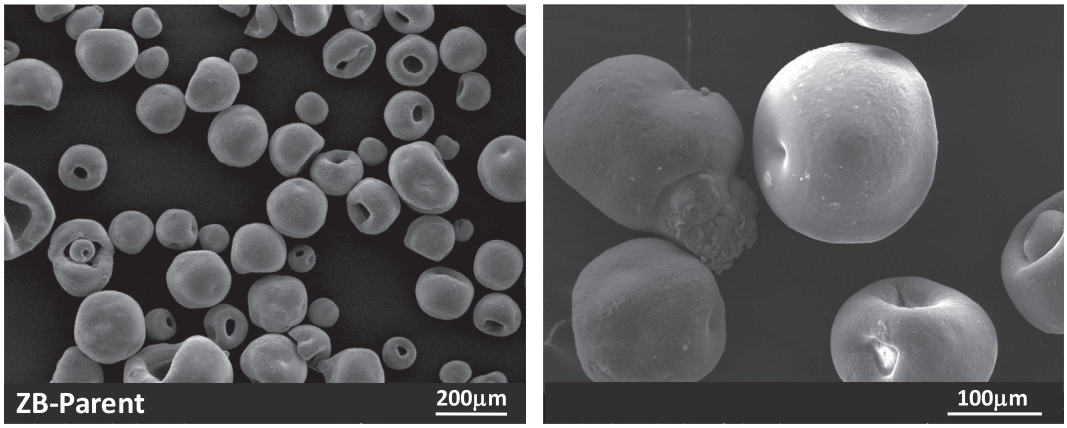

Fig. 2. SEM images of the calcined shaped catalysts before Zn incorporation (ZB-parent).

Table 2
Elemental composition of the Zn-containing samples after calcination.

Sample	Elemental analysis (wt.%)			Elemental analysis (mmol/g)		
	Al	Si	Zn	Al	Si	Zn
Z-3IE	1.0	43.6	1.0	0.36	15.52	0.16
ZB-3IE	28.3	20.0	0.53	10.5	7.12	0.08
ZB-1Zn	28.0	19.8	0.98	10.4	7.05	0.15
ZB-10Zn	25.6	18.1	8.79	9.49	6.44	1.34
B-1Zn	51.4	0.00	1.01	19.05	0.00	0.15
B-10Zn	46.0	0.00	9.12	17.05	0.00	1.39

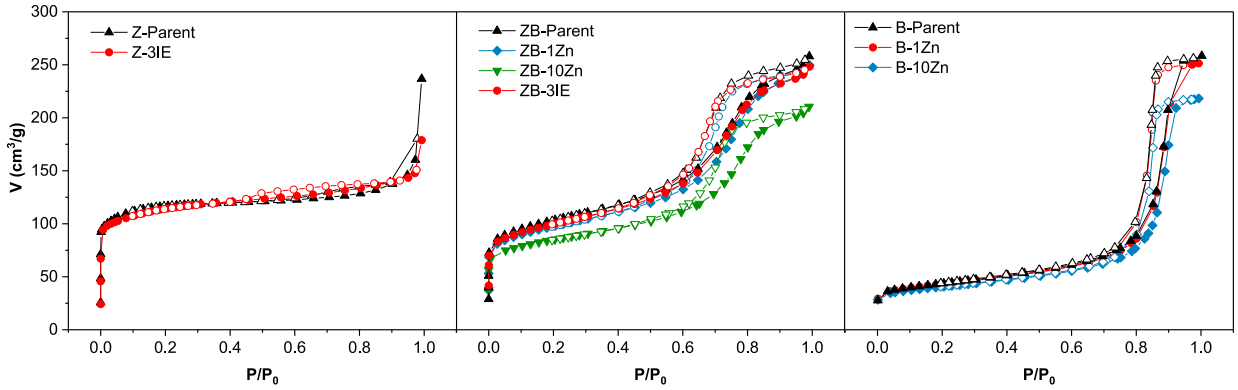

Fig. 3. Nitrogen adsorption–desorption isotherms of calcined samples with different natures (pure zeolites, shaped catalysts, and alumina) and Zn content. Solid symbols correspond to adsorption data and empty symbols to desorption.

Table 3
Surface area and pore volume of the parent and Zn-exchanged ZSM-5 samples.

Sample	Surface area (m^2/g)	Pore volume (cm^3/g)
Z-Parent	439	0.33
Z-3IE	415	0.27
ZB-Parent	307	0.38
ZB-3IE	305	0.38
ZB-1Zn	297	0.38
ZB-10Zn	250	0.32
B-Parent	94	0.39
B-1Zn	92	0.38
B-10Zn	82	0.33

It is known that the presence of Zn alters the acidic nature of zeolites, replacing protons in the exchange sites, so that the number of Lewis acid sites (LAS) increases at the expense of the number of Brønsted acid sites (BAS) [21]. To explore the effect of Zn on the acidic properties of zeolite/alumina catalysts, samples were studied by FTIR using pyridine as base probe molecule. Fig. 4 shows the spectra of the activated samples and of the samples after chemisorption of pyridine. The high-frequency regions of the spectra are nearly flat in all cases: neither the band at 3610 cm^{-1}, traditionally assigned to BAS [Si–(OH)–Al], nor the band characteristic of isolated silanols [Si–OH] is as clear for any of the shaped catalysts as for the pure zeolites. Similarly, the vibrational band corresponding to BAS after adsorption of pyridine (1544 cm^{-1}) is very small for all the shaped catalysts (Fig. 4). Such a reduction in the density of BAS for shaped catalysts is expected, and has been ascribed to the interaction of alumina with the zeolite. Unfortunately, that means that it is very difficult to identify a variation in the acidic properties upon Zn incorporation; as the number of (observable) BAS is so low in the parent, the quantification becomes unreliable. What can be clearly tracked, on the other hand, is the progressive increase in the density of LAS with incor-

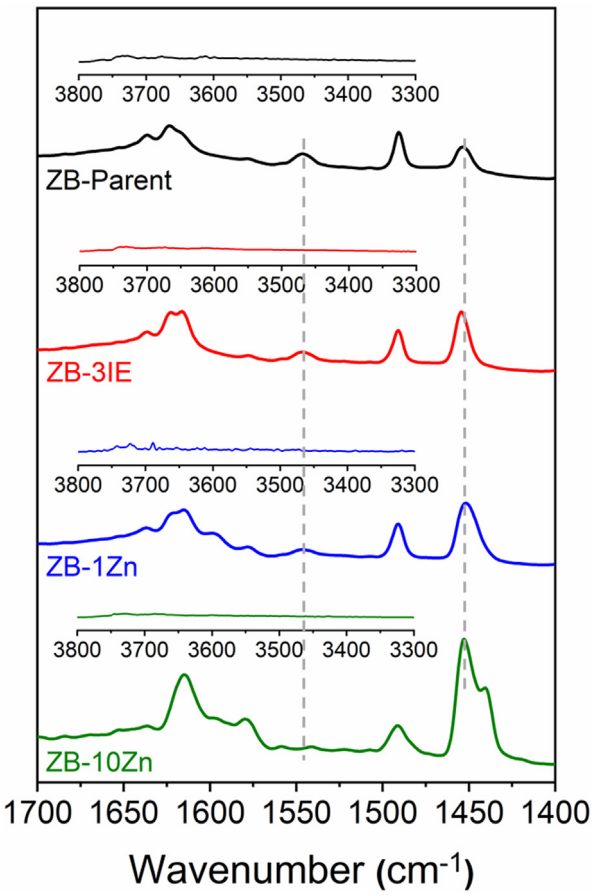

Fig. 4. FTIR spectra of the parent H-ZSM-5 and the Zn-containing HZSM-5 zeolites after dosing of pyridine and outgassing at 200 °C. The insets show the OH-stretching regions.

poration of Zn, which is clearly visible in the spectra of the samples after adsorption of pyridine (band at 1455 cm^{-1}) and becomes even clearer from the quantification data (Fig. 4, Table 4). This observation means that, similarly to what has been demonstrated for pure ZSM-5 samples, the incorporation of Zn in the shaped materials leads to the formation of new LAS, presumably active in dehydrogenation.

Further insight into the nature of these new LAS can be obtained from the shape of the associated band in the spectra of the samples after pyridine adsorption (Fig. 4). This band is quite symmetrical for the parent shaped material (ZB). However, for the impregnated sample ZB-1Zn, the band acquires a noticeable asymmetry, which turns into a clear shoulder in the case of the sample with 10% Zn (ZB-10Zn) (Fig. 4). Together with the decrease in the surface area detected in nitrogen physisorption experiments (Table 3), this can be an indicative of the presence of Zn sites other than [**Z**(Zn(OH)] (where **Z** indicates coordination to zeolite lattice oxygens close to an Al exchange site) in the impregnated samples, especially in the one with high Zn content.

Table 4
Density of acid sites detected by FTIR analysis using pyridine as base probe molecule.

	Brønsted (mmol/g)	Lewis (mmol/g)
Z-Parent	0.31	0.12
Z-3IE	0.17	0.70
ZB-Parent	0.07	0.13
ZB-3IE	0.06	0.28
ZB-1Zn	0.04	0.41
ZB-10Zn	0.01	0.99

The characterization data presented so far help us to identify the effect of the presence of Zn on the physicochemical properties of the materials. However, they do not provide information regarding the local environment or the nature of the Zn sites. To determine the Zn speciation and assess the local properties of Zn ions in the shaped catalysts (series ZB-*x*), we have employed Zn *K*-edge XAS. The technique has previously provided encouraging results in the investigation of Zn-modified pure zeolites [21,52,56–58], overcoming the difficulties often arising in connection with the "spectroscopically silent" character of Zn ions [59]. Here, through the use of an appropriate set of model systems, XAS allowed us to take a step further in resolving the complexity connected with the combined zeolite–binder system.

Fig. 5 shows an overview of the XAS results obtained for ZB type catalysts, in their as-prepared and activated state (Fig. 5b, 5d, 5f), in comparison with relevant reference spectra (Fig. 5a, 5c, 5e). The reference spectra comprise XAS data for hydrated Zn(II) ions, representative of Zn ions in the zeolite component, as well as for framework-coordinated Zn(II) species in the activated zeolite, discussed in detail in our previous work on Zn-modified neat and powdered ZSM-5 MTA catalysts [21]. Moreover, as references for Zn ions in the binder component, we considered the XAS spectra of Zn-impregnated Al_2O_3 (materials from the series B-*x*), with Zn loadings of 1 and 10 wt%, which is the same as for the investigated Zn containing ZB catalysts. Based on very similar XANES spectra reported in the previous literature [60,61], these model systems can be safely described as Zn-aluminate nanospinel phases. Here, as a function of the Zn loading, we note only subtle differences in the relative intensity of the three XANES peaks in the range 9664–9673 eV. In line with previous comparisons among Zn *K*-edge XANES of nanosized and bulk Zn-aluminate [60,61], at 1 wt % Zn-loading, smaller $ZnAl_2O_4$ aggregates should be formed than in the Zn 10 wt% case. This evidence is further corroborated by the EXAFS results in Fig. 5c and 5e. Here, the intensity of the first-shell peak stemming from Zn–O scattering contributions is substantially unchanged as a function of the Zn loading. However, all the EXAFS features at greater distances are dampened for B-1Zn with respect to B-10Zn, indicating smaller and/or more disordered $ZnAl_2O_4$ clusters at low Zn loading.

The XAS spectra of as-prepared Zn containing shaped zeolite/alumina samples revealed a mix of the characteristic features of hydrated Zn(II) hosted in the zeolite component and Zn-aluminate phases formed in the binder. The two catalysts with low Zn loading (ZB-1Zn and ZB-3IE) display very similar XAS spectra in the XANES and EXAFS regions. Conversely, the as-prepared ZB-10Zn catalyst is almost overlapped with the one of the B-10Zn model system, qualitatively indicating that, in this case, a major fraction of the total Zn in the material is located in the binder, possibly upon approaching of saturation of the available exchange sites in the zeolite.

We further examined the XAS spectra of the two low-loading ZB catalysts after activation (ZB-1Zn and ZB-3IE). In both cases, a pronounced decrease of the XANES intensity in the white-line peak region (9664–9671 eV) is observed, suggesting the conversion of hydrated Zn(II) species in the zeolite component to framework-coordinated Zn(II) moieties. Nonetheless, the characteristic fingerprints of binder-related Zn-aluminate phases (e.g., the XANES peaks at 9673 and 9687 eV, completely absent in the Z-3IE reference) are still visible, supporting the simultaneous presence of Zn species in both zeolite and binder after activation.

Starting from these qualitative insights, we turned to XANES linear combination fit (LCF) analysis to estimate the fractional contribution of different Zn species in the zeolite and binder components of the ZB catalysts. As references in our LCF analysis, we

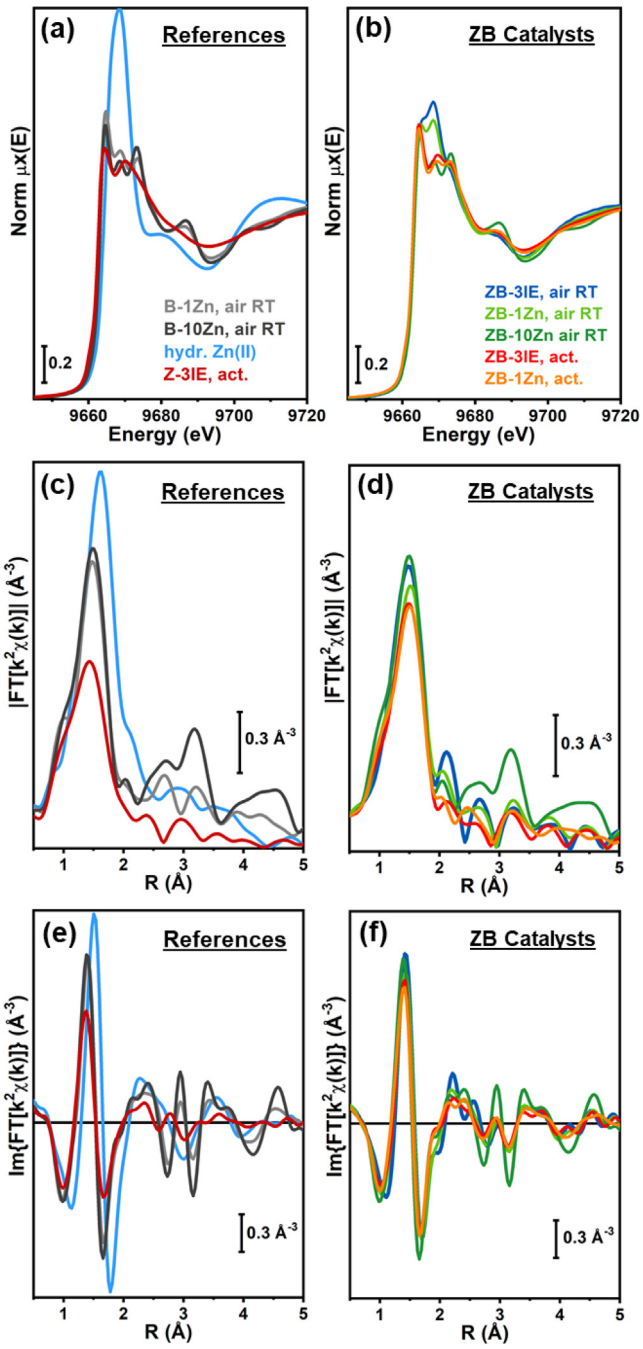

Fig. 5. Zn ***K***-edge XANES spectra of (a) selected model systems adopted as a reference in the data analysis and (b) Zn-containing catalysts belonging to the ZB series in the as-prepared and activated state. (c, d) As (a, b) but reporting the magnitude of the phase-uncorrected FT-EXAFS spectra, obtained by transforming the $\boldsymbol{k}^2$-weighted $\boldsymbol{k}^2\chi(\boldsymbol{k})$ EXAFS functions in the ***k***-space range 2.3–11.0 Å^{-1}. (e, f) As (c, d) but reporting the imaginary parts of the FT-EXAFS spectra.

employed the same model spectra as shown in Fig. 5 and discussed above (see *Experimental* for details on the fitting model). LCF results are reported in Fig. 6 and Table 5. The selected references enabled a high-quality reproduction of all the collected Zn containing zeolite/alumina XANES spectra, with *R*-factor values always lower than 3×10^{-4}. The resulting optimized fractions of Zn species are illustrated by pie charts in Fig. 6 and detailed in Table 5. As can be noted in the last column of Table 5, in all the cases the $\Sigma_i w_i$ values were comparable with unity within the corresponding LCF errors, also supporting the robustness of the fitting model.

Globally, XANES LCF results corroborate the interpretation proposed above. In particular, low-Zn-loading catalysts in their as-prepared state are well reproduced by a combination of Zn-aluminate species in the binder (accounting for ca. 60–70% of total Zn in samples prepared by IE and impregnation) and hydrated Zn (II) ions in the zeolite. Nonetheless, minor contributions from dehydrated zeolite-coordinated Zn species (modeled through the reference spectrum for activated Z-3IE) are also observed, possibly located in the innermost portions of the ZB spheres. Interestingly, this observation contrasts with what is found for powdered Zn zeolites [21], where virtually all the Zn ions occur in their hydrated form under ambient conditions. However, it can reasonably be connected with different hydrophilicity properties of the shaped ZB-catalysts with respect to the powdered-zeolite ones, possibly also influenced by the properties of Zn-aluminate phases shown to form in the binder. As-prepared ZB-10Zn is best fitted to 91% of Zn-aluminate species in the binder, with a very minor contribution of 1% hydrated Zn(II) but still ca. 8% of dehydrated, zeolite-coordinated Zn species.

Based on the XANES LCF results (giving fractions of each Zn-species over the total amount of Zn present in the sample, w_1-w_3 in Table 5) and the compositional analysis (Table 2), it is possible to estimate the absolute content of Zn in both zeolite (hydrated Zn(II) and/or dehydrated, zeolite-coordinated Zn ions) and binder (Zn-aluminate species). The results, also reported in Table 5, evidences for as-prepared low-loading ZB catalysts a similar amount of Zn hosted in the zeolite, slightly higher for ZB-1Zn (0.04 mmol/g) with respect to ZB-3IE (0.03 mmol/g). A substantial increase in the amount of Zn hosted in the zeolite, up to 0.12 mmol/g, is instead found for the most active catalyst, ZB-10Zn.

In the activated catalysts with 1 wt% Zn loading, LCF analysis reveals quite similar Zn speciation for the two samples: ca. 40% of total Zn is found to occur as binder-related $ZnAl_2O_4$, while zeolite-coordinated Zn(II) species account for the remaining ca. 60%. Not surprisingly, no trace of hydrated Zn(II) is observed under these conditions, albeit for consistency the corresponding reference spectrum was included in the LCF model. Notably, the activation procedure (see *Experimental* for details) appears to enhance the fractional contribution of Zn in the zeolite to the expenses of binder-related Zn-phases with respect to the as-prepared state. Within the LCF uncertainty (slightly higher here than for as-prepared materials) it appears plausible that migration of Zn species from the binder to the zeolite could occur upon activation, similarly to what has been documented for physical mixtures of Zn-containing oxides and zeolites upon thermal treatment [62].

Aiming to support the XAS results with a complementary proof of the presence of $ZnAl_2O_4$ phases in the Zn containing shaped materials, we have performed XRD experiments on the samples in search for crystallographic signs of the described nanospinels. Powder X-ray diffraction patterns of the samples with and without Zn are collected in Fig. 7. Pure zeolites used as reference have all the peaks characteristics of MFI samples. This does not change when Zn is added. In the case of the alumina reference samples, the XRD shows something that also remains constant upon Zn incorporation. Finally, looking at the ZB series, ZB-Parent has some of the characteristic MFI peaks, but the intensity changes, since more than half of the sample weight is alumina. Clearly, the zinc aluminate inferred from XAS is not sufficiently crystalline and/or comprises too small crystallites for detection with XRD.

3.3. Evaluation of dehydrogenation capacity of the Zn sites

It is known from previous contributions [21] that it is not only the amount of Zn but also the nature of the Zn sites and the location of the metal in the zeolite (or more importantly zeolite/binder in our case) that play crucial roles in the catalytic behavior of the

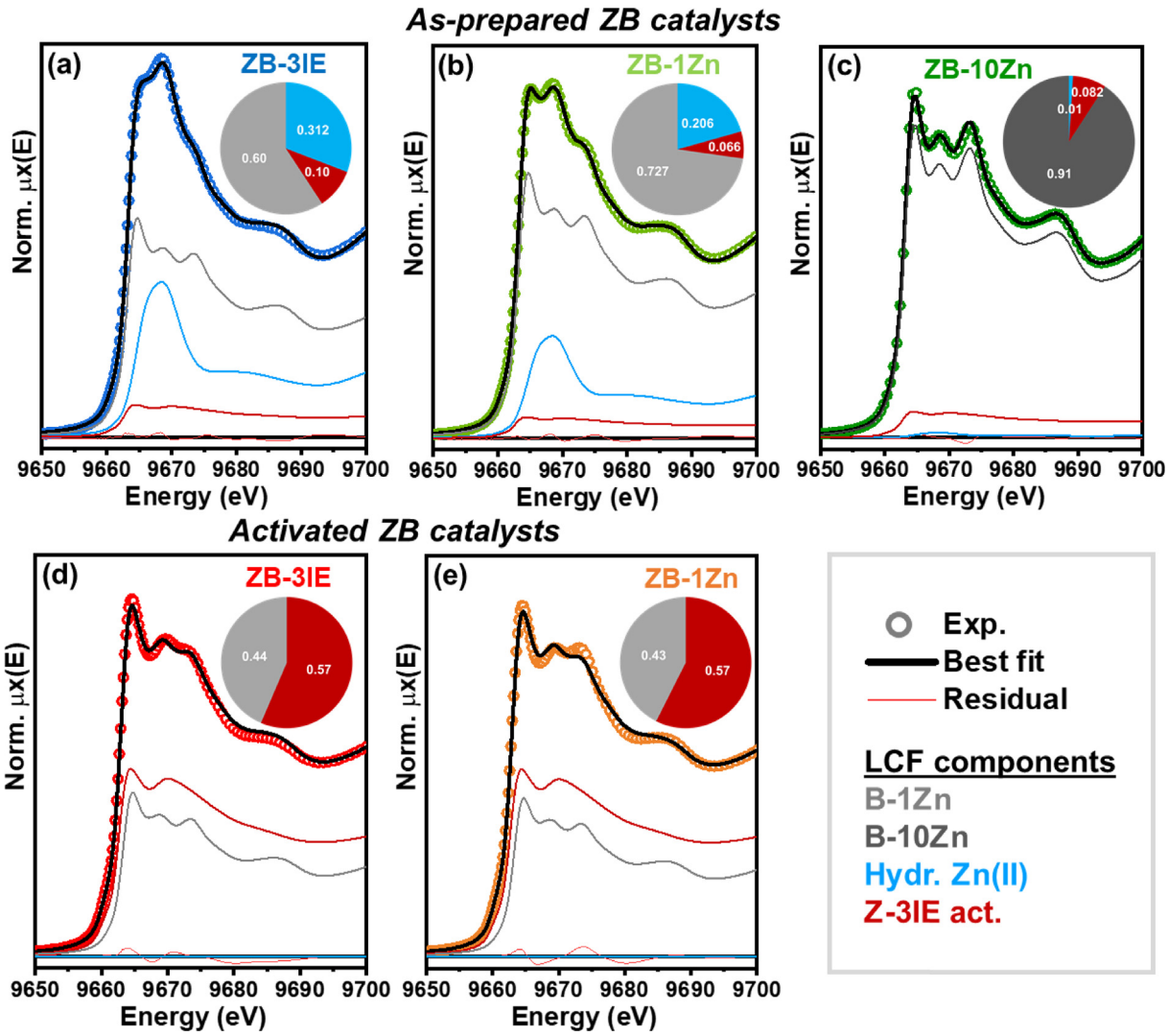

Fig. 6. Comparison between experimental (colored circles) and LCF (black solid lines) XANES spectra obtained for (a–c) as-prepared and (d, e) activated Zn-containing catalysts from the ZB series. For each analyzed sample, the LCF residuals (light red curves at the bottom of each plot) and scaled components are reported (color code: B-1Zn: gray; B-10Zn: dark gray; hydr. Zn(II): light blue; Z-3IE, act: dark red) together with pie charts illustrating the resulting Zn speciation (fractions of each Zn species over the total amount of Zn present in the samples) with the same color code.

Table 5
XANES LCF results for as-prepared and activated Zn-containing ZB catalysts. Columns in mmol/g are the result of the combination of the LCF results and the total Zn content measured for the samples (see Table 2).

As-prepared ZB catalysts (RT, air)						
Sample	w_1: hyd. Zn(II)	w_2: Z-3IE	w_3: B-1Zn/B-10Zn	*R*-factor	Zn in Z (mmol/g)[a]	Zn in B (mmol/g)[b]
ZB-3IE	0.312 ± 0.003	0.10 ± 0.01	0.60 ± 0.01	1.0×10^{-4}	0.03	0.05
ZB-1Zn	0.206 ± 0.002	0.066 ± 0.007	0.727 ± 0.008	0.6×10^{-4}	0.04	0.11
ZB-10Zn	0.010 ± 0.002	0.082 ± 0.01	0.91 ± 0.01	0.6×10^{-4}	0.12	1.22
Activated ZB catalysts (act. O_2 400 °C, measured at RT)						
Sample	w_1: hyd. Zn(II)	w_2: Z-3IE	w_3: B-1Zn	*R*-factor	Zn in Z(mmol/g)[a]	Zn in B (mmol/g)[b]
ZB-3IE	0.00 ± 0.02	0.57 ± 0.01	0.44 ± 0.01	2.2×10^{-4}	0.05	0.03
ZB-1Zn	0.00 ± 0.02	0.57 ± 0.02	0.43 ± 0.02	2.7×10^{-4}	0.09	0.06

[a] Calculated as (w_1 + w_2) × total Zn content (mmol/g) determined by ICP-OES for each sample (Table 2).
[b] Calculated as w_3 × total Zn content (mmol/g) determined by ICP-OES for each sample (Table 2).

samples when used as MTA catalysts. The presence of Zn enhances the formation of aromatics and molecular hydrogen due to the extra dehydrogenation capacity that it confers on the catalyst. However, MTA is a quite complex process in which many chemical transformations are taking place at the same time, and it is not straightforward to extract information about single reaction steps from the overall MTA performance discussed in Section 3.1. Thus, in order to simplify the study and to gain more specific information, we decided to use alternative reactants for the comparison of Zn dehydrogenation capacity: cyclohexane and 1-heptene. The experiments were done as described in Section 2.3, keeping a similar partial pressure of carbon for all the experiments. Both a cyclic

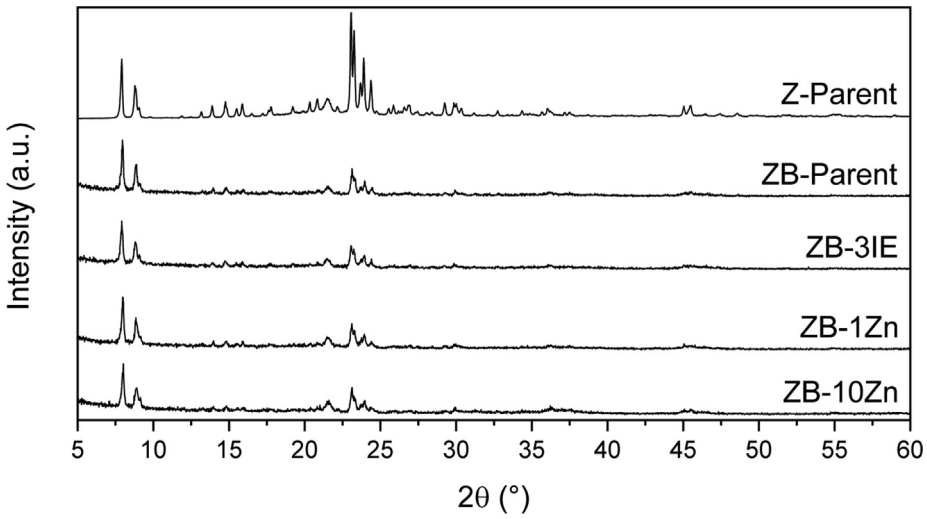

Fig. 7. Powder X-ray diffraction patterns of the reference parent zeolite and the calcined shaped materials (pure alumina and zeolite/alumina solids) with different Zn incorporation type and content.

and a noncyclic reactant were employed, as the sequence of dehydrogenation and cyclization is unknown. The first observation is that under similar reaction conditions, the conversion of 1-heptene is generally higher than the conversion of cyclohexane (Figs. 8 and 9). This might be reasonable considering that the reactivity of alkenes is generally higher than the reactivity of cycloalkanes.

Looking at the cyclohexane conversion obtained with the different catalysts, is clear that pure zeolites are in most cases more active than the shaped catalysts. This is intuitive, considering that only 40% of the weight of the shaped catalysts is the active phase. For the shaped materials to be more active than the pure zeolite, a large amount of Zn is necessary; the sample with 10% Zn is the only one resulting in higher conversion than the pure zeolite (Fig. 8). We attribute this to the high concentration of LAS upon extensive Zn incorporation (Table 4).

Turning now to the product distributions, it should be realized that a catalyst with only dehydrogenation capacity would produce benzene as the main reaction product. However, the Brønsted acid sites of the zeolite can catalyze other reactions, such as cracking, methylation, and hydrogen transfer, giving a wider distribution of products. Looking at the product distribution (Fig. 10) both for the pure zeolites and for the shaped catalysts, there is an increase in the production of aromatics comparing parent samples and samples with Zn. This increase is quite dramatic in the case of the sample Z-3IE, for which most of the products are aromatics. In this catalyst, there is no indication of Zn environments other than **Z**

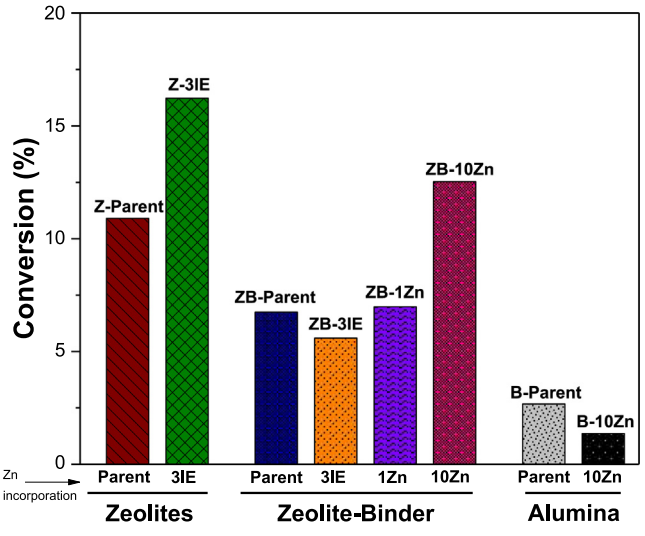

Fig. 8. Conversion of cyclohexane. Reaction temperature is 400 °C, cyclohexane partial pressure is 43 mbar, total pressure is atmospheric, and WHSV = 1.7 h^{-1}. Results collected after 5 min on stream.

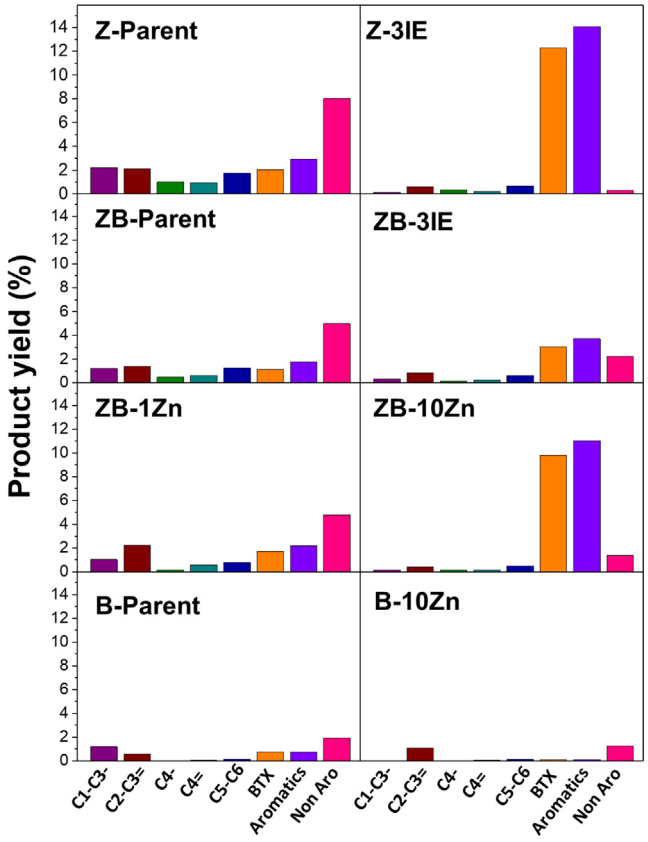

Fig. 9. Product yields during the conversion of cyclohexane. Reaction temperature is 400 °C, cyclohexane partial pressure is 43 mbar, total pressure is atmospheric, and WHSV = 1.7 h^{-1}. Results collected after 5 min on stream.

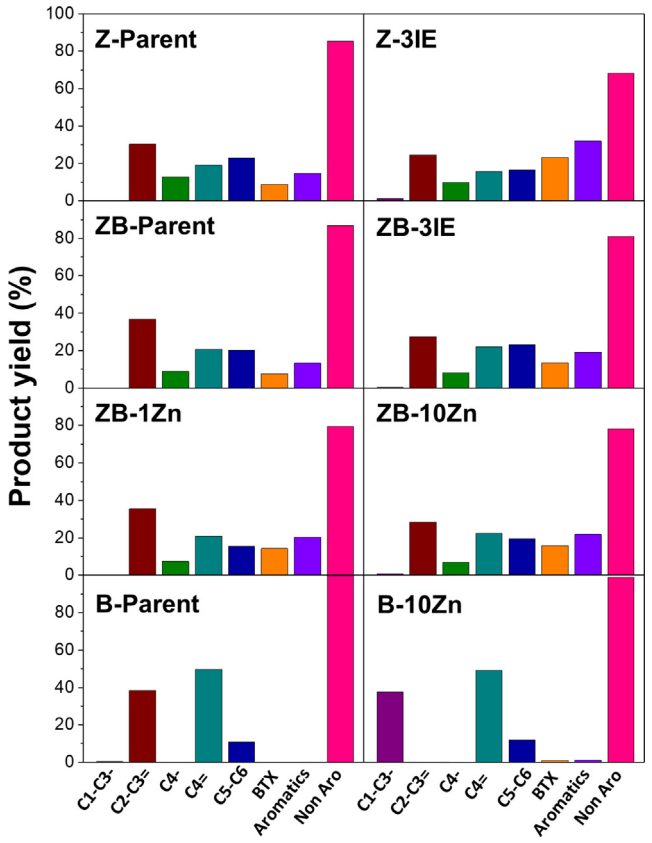

Fig. 10. Product yields during the conversion of 1-heptene. Reaction temperature is 400 °C, cyclohexane partial pressure is 37 mbar, total pressure is atmospheric, and WHSV = 2.0 h^{-1}. Results collected after 5 min on stream.

[Zn(OH)] (ion exchange sites) [21], which are considered very active as dehydrogenating agents. For the shaped materials, for which the situation becomes more complicated, the effect of Zn is dependent not only on the Zn content but also on the preparation method and the type of Zn sites in the material. In this sense, even if sample ZB-1Zn contains a larger amount of Zn than ZB-3IE, the impregnated shaped catalyst produces less aromatics and more of the short-chain nonaromatic products (Fig. 10), demonstrating that the location of the Zn and the kind of interaction with the zeolite or the binder also play a role. In sample ZB-3IE most of the Zn is incorporated as **Z[**Zn(OH)] species, as it does in a pure zeolite, whereas the distribution of sites could be different in the case of ZB-1Zn for which the metal is initially to a larger degree located in the binder (Fig. 6). However, ZB-10Zn displays very high selectivity toward aromatics, comparable to that of Z-3IE. This indeed suggests that the majority of the ion exchange sites are occupied by Zn also for this catalysts, in line with XANES LCF results (Fig. 6 and Table 5). Finally, it may be noted that binder and impregnated binder display very low activity, as one might expect for a material without any zeolite component present. Clearly, neither the regular zeolite Brønsted acid sites nor the active Zn species (Zn located in the exchange positions of the zeolite crystals) can be formed in this type of material.

In the case of the conversion of 1-heptene, all the samples are very active, showing conversion levels very close to 100% (not shown), rendering comparisons of activities impossible. Unlike the case of cyclohexane, when feeding 1-heptene, the main reaction products are C_2–C_4 olefins (Fig. 9). It is, however, possible to evaluate the variations in the dehydrogenation and the cyclization capacity of the catalysts by analyzing the aromatics yields. Essentially, the same observations as seen for cyclohexane feed can be made, albeit much less clearly so. However, the production of aromatics does increase slightly in the presence of Zn both for the pure zeolites and for the shaped catalysts. When using pure alumina (series B-*x*) as catalysts, nearly only cracking products are obtained, possibly suggesting that the $ZnAl_2O_4$ spinel phase in the binder induces very limited (dehydrogenation) activity, at least in the absence of proximal BAS.

4. Conclusions

A series of Zn-loaded shaped ZSM-5/alumina catalysts for the conversion of methanol to aromatics have been investigated. Only a moderate increase in the aromatics yield is seen at total pressure 20 bar upon Zn incorporation, but the catalyst lifetime is substantially increased, and the mode of hydrogen transfer is profoundly shifted from paraffin formation to formation of molecular hydrogen. The best catalyst is prepared by impregnating 10 wt% Zn onto the shaped material. Using a combination of characterization techniques, it has been possible to distinguish between Zn species located in the zeolite component and in the binder. At low Zn loading, ion exchange of the shaped material leads primarily to Zn species in ion exchange positions, whereas the more scalable and practical process of impregnation of already shaped material results in a larger fraction of Zn located in the binder. However, after calcination the situation is comparable, suggesting that the metal can migrate to the exchange sites during activation. For the catalysts prepared by impregnation, a high Zn loading is required for optimum catalyst performance with respect to lifetime. A high dehydrogenation capacity at high Zn loadings demonstrates that the ion-exchange sites in the zeolite become saturated with Zn species when excess Zn is employed during impregnation. For both ion exchange and impregnation, the Zn not present in the zeolite is distributed within the binder as small/disordered $ZnAl_2O_4$ clusters not observable by X-ray diffraction.

Declaration of Competing Interest

The authors declare that they have no known competing financial interests or personal relationships that could have appeared to influence the work reported in this paper.

Acknowledgments

This work has been partially supported by the Innovation Fund Denmark (Ref. 5190-00019B). I. Pinilla-Herrero acknowledges this institution for the concession of an industrial postdoc contract. Dr. Jingxiu Xie is acknowledged for setting up the gas chromatograph used to provide the data in the Supplementary Material.

Appendix A. Supplementary data

Supplementary data to this article can be found online at https://doi.org/10.1016/j.jcat.2020.10.024.

References

[1] E.T.C. Vogt, G.T. Whiting, A. Dutta Chowdhury, B.M. Weckhuysen, Chapter Two - Zeolites and Zeotypes for Oil and Gas Conversion, in: C.J. Friederike (Ed.) Adv. Cataly. 2015, pp. 143–314.
[2] C.S. Cundy, P.A. Cox, The Hydrothermal Synthesis of Zeolites: History and Development from the Earliest Days to the Present Time, Chem. Rev. 103 (2003) 663–702.
[3] M.E. Davis, Ordered porous materials for emerging applications, Nature 417 (2002) 813–821.
[4] A. Primo, H. Garcia, Zeolites as catalysts in oil refining, Chem. Soc. Rev. 43 (2014) 7548–7561.

[5] C. Martínez, A. Corma, Inorganic molecular sieves: Preparation, modification and industrial application in catalytic processes, Coord. Chem. Rev. 255 (2011) 1558–1580.
[6] S. Mintova, J. Grand, V. Valtchev, Nanosized zeolites: Quo Vadis?, C.R. Chim. 19 (2016) 183–191.
[7] U. Olsbye, S. Svelle, M. Bjørgen, P. Beato, T.V.W. Janssens, F. Joensen, S. Bordiga, K.P. Lillerud, Conversion of Methanol to Hydrocarbons: How Zeolite Cavity and Pore Size Controls Product Selectivity, Angew. Chem. Int Ed. 51 (2012) 5810–5831.
[8] M. Stöcker, Methanol-to-hydrocarbons: catalytic materials and their behavior1, Micropor. Mesopor. Mater. 29 (1999) 3–48.
[9] A. Galadima, O. Muraza, Recent Developments on Silicoaluminates and Silicoaluminophosphates in the Methanol-to-Propylene Reaction: A Mini Review, Ind. Eng. Chem. Res. 54 (2015) 4891–4905.
[10] A.M. Niziolek, O. Onel, Y.A. Guzman, C.A. Floudas, Biomass-Based Production of Benzene, Toluene, and Xylenes via Methanol: Process Synthesis and Deterministic Global Optimization, Energy Fuels 30 (2016) 4970–4998.
[11] G. Leonzio, State of art and perspectives about the production of methanol, dimethyl ether and syngas by carbon dioxide hydrogenation, J. CO_2 Util. 27 (2018) 326–354.
[12] S. Kar, J. Kothandaraman, A. Goeppert, G.K.S. Prakash, Advances in catalytic homogeneous hydrogenation of carbon dioxide to methanol, J. CO_2 Util. 23 (2018) 212–218.
[13] M. Martín, Artificial versus Natural Reuse of CO2 for DME Production: Are We Any Closer?, Engineering 3 (2017) 166–170.
[14] D. Xiang, Y. Qian, Y. Man, S. Yang, Techno-economic analysis of the coal-to-olefins process in comparison with the oil-to-olefins process, Appl. Energy 113 (2014) 639–647.
[15] M. Bender, New Technologies and Alternative Feedstocks in Petrochemistry and Refining, Dresden, Germany, 2013.
[16] E. Lalik, X. Liu, J. Klinowski, Role of gallium in the catalytic activity of zeolite [Si, Ga]-ZSM-5 for methanol conversion, J. Phys. Chem. 96 (1992) 805–809.
[17] Y. Ono, K. Kanae, Transformation of butanes over ZSM-5 zeolites. Part 2. - Formation of aromatic hydrocarbons over Zn-ZSM-5 and Ga-ZSM-5, Jo. Chem. Soc. Faraday Trans. 87 (1991) 669–675.
[18] M. Conte, J.A. Lopez-Sanchez, Q. He, D.J. Morgan, Y. Ryabenkova, J.K. Bartley, A. F. Carley, S.H. Taylor, C.J. Kiely, K. Khalid, G.J. Hutchings, Modified zeolite ZSM-5 for the methanol to aromatics reaction, Catal. Sci. Technol. 2 (2012) 105–112.
[19] R. Barthos, T. Bánsági, T. Süli Zakar, F. Solymosi, Aromatization of methanol and methylation of benzene over Mo2C/ZSM-5 catalysts, J. Catal. 247 (2007) 368–378.
[20] J. Zhang, W. Qian, C. Kong, F. Wei, Increasing para-Xylene Selectivity in Making Aromatics from Methanol with a Surface-Modified Zn/P/ZSM-5 Catalyst, ACS Catal. 5 (2015) 2982–2988.
[21] I. Pinilla-Herrero, E. Borfecchia, J. Holzinger, U.V. Mentzel, F. Joensen, K.A. Lomachenko, S. Bordiga, C. Lamberti, G. Berlier, U. Olsbye, S. Svelle, J. Skibsted, P. Beato, High Zn/Al ratios enhance dehydrogenation vs hydrogen transfer reactions of Zn-ZSM-5 catalytic systems in methanol conversion to aromatics, J. Catal. 362 (2018) 146–163.
[22] P. Tian, Y. Wei, M. Ye, Z. Liu, Methanol to Olefins (MTO): From Fundamentals to Commercialization, ACS Catal. 5 (2015) 1922–1938.
[23] F.J. Keil, Methanol-to-hydrocarbons: process technology, Micropor. Mesopor. Mater. 29 (1999) 49–66.
[24] S.W. Kaiser, U.S. Patent 4 499 327, 1985.
[25] B.V. Vora, T.L. Marker, P.T. Barger, H.R. Nilsen, S. Kvisle, T. Fuglerud, Stud. Surf. Scie. Catal. 107 (1997) 87.
[26] J.Q. Chen, A. Bozzano, B. Glover, T. Fuglerud, S. Kvisle, Recent advancements in ethylene and propylene production using the UOP/Hydro MTO process, Catal. Today 106 (2005) 103–107.
[27] D. Xiang, S. Yang, Z. Mai, Y. Qian, Comparative study of coal, natural gas, and coke-oven gas based methanol to olefins processes in China, Comput. Chem. Eng. 83 (2015) 176–185.
[28] I. Pinilla-Herrero, U. Olsbye, C. Márquez-Álvarez, E. Sastre, Effect of framework topology of SAPO catalysts on selectivity and deactivation profile in the methanol-to-olefins reaction, J. Catal. 352 (2017) 191–207.
[29] J.S. Martinez-Espin, M. Morten, T.V.W. Janssens, S. Svelle, P. Beato, U. Olsbye, New insights in catalyst deactivation and product distribution of zeolites in the Methanol-To-Hydrocarbons, MTH) reaction with methanol and dimethyl ether feeds, Catal. Sci. & Technol., 2017.
[30] J.S. Martínez-Espín, K. De Wispelaere, T.V.W. Janssens, S. Svelle, K.P. Lillerud, P. Beato, V. Van Speybroeck, U. Olsbye, Hydrogen Transfer versus Methylation: On the Genesis of Aromatics Formation in the Methanol-To-Hydrocarbons Reaction over H-ZSM-5, ACS Catal. 7 (2017) 5773–5780.
[31] B. Liu, B. Yao, S. Gonzalez-Cortes, V.L. Kuznetsov, M. AlKinany, S.A. Aldrees, T. Xiao, P.P. Edwards, A research into the thermodynamics of methanol to hydrocarbon (MTH): conflictions between simulated product distribution and experimental results, Appl. Petrochem. Res. 7 (2017) 55–66.
[32] L. Zhang, Y. Huang, New Insights into Formation of Molecular Sieve SAPO-34 for MTO Reactions, J. Phys. Chem. C 120 (2016) 25945–25957.
[33] I. Yarulina, J. Goetze, C. Gucuyener, L. van Thiel, A. Dikhtiarenko, J. Ruiz-Martinez, B.M. Weckhuysen, J. Gascon, F. Kapteijn, Methanol-to-olefins process over zeolite catalysts with DDR topology: effect of composition and structural defects on catalytic performance, Catal. Sci. Technol. 6 (2016) 2663–2678.
[34] S. Müller, Y. Liu, F.M. Kirchberger, M. Tonigold, M. Sanchez-Sanchez, J.A. Lercher, Hydrogen Transfer Pathways during Zeolite Catalyzed Methanol Conversion to Hydrocarbons, J. Am. Chem. Soc. 138 (2016) 15994–16003.
[35] R. Martinez-Franco, Z. Li, J. Martinez-Triguero, M. Moliner, A. Corma, Improving the catalytic performance of SAPO-18 for the methanol-to-olefins (MTO) reaction by controlling the Si distribution and crystal size, Catal. Sci. Technol. 6 (2016) 2796–2806.
[36] S.N. Khadzhiev, M.V. Magomedova, E.G. Peresypkina, Kinetic models of methanol and dimethyl ether conversion to olefins over zeolite catalysts (Review), Pet. Chem. 55 (2015) 503–521.
[37] U. Olsbye, S. Svelle, K.P. Lillerud, Z.H. Wei, Y.Y. Chen, J.F. Li, J.G. Wang, W.B. Fan, The formation and degradation of active species during methanol conversion over protonated zeotype catalysts, Chem. Soc. Rev. 44 (2015) 7155–7176.
[38] D. Rojo-Gama, M. Signorile, F. Bonino, S. Bordiga, U. Olsbye, K.P. Lillerud, P. Beato, S. Svelle, Structure–deactivation relationships in zeolites during the methanol–to-hydrocarbons reaction: Complementary assessments of the coke content, J.f Catal. 351 (2017) 33–48.
[39] S. Afandizadeh, E.A. Foumeny, Design of packed bed reactors: guides to catalyst shape, size, and loading selection, Appl. Therm. Eng. 21 (2001) 669–682.
[40] S. Mitchell, N.-L. Michels, J. Pérez-Ramírez, From powder to technical body: the undervalued science of catalyst scale up, Chem. Soc. Rev. 42 (2013) 6094–6112.
[41] J.S.J. Hargreaves, A.L. Munnoch, A survey of the influence of binders in zeolite catalysis, Catal. Sci. Technol. 3 (2013) 1165–1171.
[42] A. Martin, H. Berndt, U. Lohse, U. Wolf, Effect of Si : Al ratio and type of binder on the catalytic properties of HZSM-5 catalysts, J. Chem.l Soc, Faraday Trans. 89 (1993) 1277–1282.
[43] N.-L. Michels, S. Mitchell, J. Pérez-Ramírez, Effects of Binders on the Performance of Shaped Hierarchical MFI Zeolites in Methanol-to-Hydrocarbons, ACS Catal. 4 (2014) 2409–2417.
[44] T. Shoinkhorova, A. Dikhtiarenko, A. Ramirez, A. Dutta Chowdhury, M. Caglayan, J. Vittenet, A. Bendjeriou-Sedjerari, O.S. Ali, I. Morales-Osorio, W. Xu, J. Gascon, Shaping of ZSM-5-Based Catalysts via Spray Drying: Effect on Methanol-to-Olefins Performance, ACS Appl, Mater. Interfaces 11 (2019) 44133–44143.
[45] X. Niu, J. Gao, Q. Miao, M. Dong, G. Wang, W. Fan, Z. Qin, J. Wang, Influence of preparation method on the performance of Zn-containing HZSM-5 catalysts in methanol-to-aromatics, Micropor. Mesopor. Mater. 197 (2014) 252–261.
[46] K.K. Matthias Thommes, A.V. Neimark, J.P. Olivier, F. Rodriguez-Reinoso, J. Rouquerol, K.S.W. Sing, Physisorption of gases, with special reference to the evaluation of surface area and pore size distribution (IUPAC Technical Report), Pure Appl. Chem. 87 (2015) 1051–1069.
[47] B.C. Lippens, B.G. Linsen, J.H.D. Boer, Studies on pore systems in catalysts I. The adsorption of nitrogen; apparatus and calculation, J. Catal. 3 (1964) 32–37.
[48] E. Selli, L. Forni, Comparison between the surface acidity of solid catalysts determined by TPD and FTIR analysis of pre-adsorbed pyridine, Micropor. Mesopor. Mater. 31 (1999) 129–140.
[49] O. Mathon, A. Beteva, J. Borrel, D. Bugnazet, S. Gatla, R. Hino, I. Kantor, T. Mairs, M. Munoz, S. Pasternak, F. Perrin, S. Pascarelli, The time-resolved and extreme conditions XAS (TEXAS) facility at the European Synchrotron Radiation Facility: the general-purpose EXAFS bending-magnet beamline BM23, J. Synchrotron Radiat. 22 (2015) 1548–1554.
[50] S. Bordiga, E. Groppo, G. Agostini, J.A. van Bokhoven, C. Lamberti, Reactivity of Surface Species in Heterogeneous Catalysts Probed by In Situ X-ray Absorption Techniques, Chem. Rev. 113 (2013) 1736–1850.
[51] B. Ravel, M. Newville, ATHENA, ARTEMIS, HEPHAESTUS: data analysis for X-ray absorption spectroscopy using IFEFFIT, J. Synchrotron Radiat. 12 (2005) 537–541.
[52] E. Morra, G. Berlier, E. Borfecchia, S. Bordiga, P. Beato, M. Chiesa, Electronic and Geometrical Structure of Zn+ Ions Stabilized in the Porous Structure of Zn-Loaded Zeolite H-ZSM-5: A Multifrequency CW and Pulse EPR Study, J. Phys. Chem. C 121 (2017) 14238–14245.
[53] S.S. Arora, D.L.S. Nieskens, A. Malek, A. Bhan, Lifetime improvement in methanol-to-olefins catalysis over chabazite materials by high-pressure H2 co-feeds, Nat. Catal. 1 (2018) 666–672.
[54] X. Zhao, J. Li, P. Tian, L. Wang, X. Li, S. Lin, X. Guo, Z. Liu, Achieving a Superlong Lifetime in the Zeolite-Catalyzed MTO Reaction under High Pressure: Synergistic Effect of Hydrogen and Water, ACS Catal. 9 (2019) 3017–3025.
[55] K.S.W. Sing, D.H. Everett, R.A.W. Haul, L. Moscou, R.A. Pierotti, J. Rouquerol, T. Siemieniewska, Reporting Physisorption Data for Gas/Solid Systems with Special Reference to the Determination of Surface Area and Porosity, Pure Appl. Chem. 57 (1985) 603–619.
[56] J.A. Biscardi, G.D. Meitzner, E. Iglesia, Structure and Density of Active Zn Species in Zn/H-ZSM5 Propane Aromatization Catalysts, J. Catal. 179 (1998) 192–202.
[57] S.M.T. Almutairi, B. Mezari, P.C.M.M. Magusin, E.A. Pidko, E.J.M. Hensen, Structure and Reactivity of Zn-Modified ZSM-5 Zeolites: The Importance of Clustered Cationic Zn Complexes, ACS Catal. 2 (2012) 71–83.
[58] A. Oda, T. Ohkubo, T. Yumura, H. Kobayashi, Y. Kuroda, Synthesis of an unexpected [Zn2]2+ species utilizing an MFI-type zeolite as a nano-reaction pot and its manipulation with light and heat, Dalton Trans. 44 (2015) 10038–10047.
[59] J.E. Penner-Hahn, Characterization of “spectroscopically quiet” metals in biology, Coordi. Chem. Rev. 249 (2005) 161–177.

[60] R. Revel, D. Bazin, E. Elkaim, Y. Kihn, H. Dexpert, An in Situ Study Using Anomalous Wide-Angle X-ray Scattering and X-ray Absorption Spectroscopy of the Catalytic System ZnAl2O4 Supported on Alumina, J. Phys. Chem. B 104 (2000) 9828–9835.
[61] F. Tielens, D. Bazin, Operando characterization and DFT modelling of nanospinels: Some examples showing the relationship with catalytic activity, Appl. Catal. A Gen. 504 (2015) 631–641.
[62] C. Ahoba-Sam, E. Borfecchia, A. Lazzarini, A. Bugaev, A.A. Isah, M. Taoufik, S. Bordiga, U. Olsbye, On the conversion of CO2 to value added products over composite PdZn and H-ZSM-5 catalysts: excess Zn over Pd, a compromise or a penalty?, Catal Sci, Technol, 2020.